Contents lists available at ScienceDirect

Remote Sensing of Environment

journal homepage: www.elsevier.com/locate/rse

Soil moisture retrieval from Sentinel-1 using a first-order radiative transfer model—A case-study over the Po-Valley

Raphael Quast [*], Wolfgang Wagner, Bernhard Bauer-Marschallinger, Mariette Vreugdenhil

TU Wien, Department of Geodesy and Geoinformation, Vienna, Austria

ARTICLE INFO

ABSTRACT

Soil moisture is an important variable controlling many land surface processes and is used to quantify precipitation, drought, flooding, irrigation and other factors that influence decision making and risk-assessment. This paper presents the retrieval of high resolution (~1 km) soil moisture data from Sentinel-1 C-band Synthetic Aperture Radar (SAR) backscatter measurements using a new bistatic radiative transfer modeling framework (RT1) previously only tested for scatterometer data. The model is applied over a diverse set of landcover types across the entire Po-Valley in Italy over a 4-year time-period from 2016 to 2019. The performance of the soil moisture retrievals is analyzed with respect to the ERA5-Land reanalysis dataset. The model parameterisation and retrieval method are chosen such as to constitute a trade-off between a physically plausible and a computationally feasible modeling approach. The results demonstrate the potential of RT1 for the retrieval of high-resolution soil moisture data from SAR time series.

1. Introduction

Soil moisture, recognized by the Global Climate Observation System (GCOS) as an "Essential Climate Variable" (Bojinski et al., 2014; Hollmann et al., 2013), is an important input-variable for studies and applications concerning hydrology, agriculture, soil-sciences and global climate models (Peng et al., 2021). It can be observed using active and passive microwave satellites, on regional to global scales, irrespective of cloud-coverage and lightning conditions, and feasible even in the presence of low to moderate vegetation coverage (Romshoo et al., 2002).

While coarse resolution (~10–50 km) soil moisture (SM) data derived from microwave radiometers and scatterometers (for example SMOS (Kerr et al., 2001), SMAP (Entekhabi et al., 2010), and AS-CAT (Wagner et al., 2013)) are capable of providing valuable insights for large-scale numerical weather prediction and climate models, these data sets do not capture local scale soil moisture variations. Many small-scale applications such as localized weather prediction, risk- and disaster management as well as applications in hydrology, forestry and agriculture require a minimal spatial resolution below 1 km to adequately represent the local conditions ultimately desired by the end-users (Peng et al., 2021). Such a high spatial resolution can be achieved using Synthetic Aperture Radar (SAR) instruments like the C-band SAR on board the ESA Copernicus Sentinel-1 satellite constellation (S1A and S1B and their upcoming successors S1C and S1D). Compared to other SAR sensors (Balenzano et al., 2021), Sentinel-1 is particularly attractive for soil moisture monitoring because of its good temporal coverage. However, the Sentinel-1 dataset has unique sampling and measurements characteristics that require the adaption of existing retrieval strategies (Bauer-Marschallinger et al., 2019; Gao et al., 2017; Foucras et al., 2020; Nguyen et al., 2021; Benninga et al., 2019; Zhu et al., 2022; Mengen et al., 2023).

In addition, it has also been shown that data-fusion methods can be used to harness the good temporal and radiometric resolution of coarse-scale observations and the fine spatial details provided by SAR systems. For example, the Copernicus 1 km Soil Water Index (SWI) dataset (Bauer-Marschallinger et al., 2018) fuses observations from the ASCAT instrument (active C-band radar, ~25 km) and Sentinel-1 (~1 km) and the "SMAP/Sentinel-1" (Das et al., 2020) product uses a fusion between SMAP (passive L-band radiometer, ~33 km) and Sentinel-1 (~1 km) to generate high-resolution soil moisture products at 1 and 3 km sampling. While these fusion approaches provide a unique way to obtain datasets with fine spatio-temporal sampling, the temporal signal is mostly driven by the much more frequent coarse scale observations. Also the effective spatial resolution of a fused dataset is likely larger than that of the SAR data that were used to superimpose the fine spatial details. Small-scale soil moisture patterns caused by irrigation or highly localized precipitation may not be captured by these datasets. Therefore, it is important to develop high resolution data sets just based upon Sentinel-1 observations, even if their temporal sampling falls short of the fused data sets.

The aim of this study was to investigate the use of the new radiative transfer model RT1 for retrieving soil moisture from Sentinel-1 SAR time series at 1 km scale. RT1 introduces parametric distribution functions to simulate the directional dependency of soil- and vegetation scattering (Quast and Wagner, 2016), thus representing a generic scattering model capable of simulating not just backscatter as needed by mono-static radar systems but also bistatic scattering needed for multi-satellite measurement concepts as realized by Global Navigation Satellite System (GNSS) Reflectometry (Edokossi et al., 2020) and the upcoming SAR constellation mission Harmony (ESA, 2022). While providing a rather flexible framework, the parametrization of RT1 is challenging. Therefore, studies are needed to test its applicability for different radar instruments. In Quast et al. (2019) we have already shown that RT1 is well suited for simulating Advanced Scatterometer (ASCAT) backscatter measurements at 25 km spatial resolution over the entire incidence angle range from 25° to 65°. The parametrization of RT1 profited from the multiple-viewing capabilities of the ASCAT instrument, and allowed to separate scattering contributions from the soil surface, the layer of vegetation and soil–vegetation interactions.

Other than ASCAT, the Sentinel-1 SAR instrument provides a much finer spatial resolution but also entails measurement characteristics which complicate the separation of soil- and vegetation scattering contributions: A lower temporal resolution, a lower radiometric accuracy, a narrower range of incidence-angles and only a single incidence-angle per observation. To overcome these limitations, we investigate the use of auxiliary Leaf Area Index (LAI) data to serve as a proxy for the seasonal dynamics of the vegetation layer within the RT1 retrieval. The presented model parametrization is hereby applied over a variety of landcover-types in the Po-Valley basin (Italy) for a set of ~300000 timeseries (2016–2019) at an effective spatial resolution of ~1 km (500 m pixel sampling).

The presented work is structured as follows: Section 2 provides a description of the used methods as well as the RT1 model parametrization and Section 3 presents details on the used datasets. Finally, Section 4 provides a comprehensive discussion on the constraints that led to the used model-parametrization and gives an overview of the obtained results and their performance in comparison to the ERA5-Land reanalysis dataset (ECMWF, 2018).

All results presented within this paper have been generated with the RT1-python module which is available as an open-source package (Quast, 2021).

2. Methods

2.1. RT1 model

A key task for radar-based soil moisture retrievals is the separation of measured backscatter (σ^0) data into contributions originating from soil- and vegetation (Fung, 1994; Ulaby et al., 1986). In the presented study, this separation is performed by using a first-order radiative transfer model (RT1) (Quast et al., 2019) in conjunction with a non-linear least squares optimization routine. The scattering response of a vegetation-covered surface is described via successive orders of scattering expansions of the radiative transfer equation applied to the problem of a (rough) surface covered by a tenuous distribution of particulate media. The primary assumption is that any radiation which is scattered more than once inside the vegetation-layer no longer adds a significant contribution to the signal measured by the detector. This approximation leads to a so-called $\omega - \tau$ model (Attema and Ulaby, 1978), where the single-particle properties used in radiative transfer theory (scattering-coefficient κ_s, extinction-coefficient κ_{ex}...) are embedded in the **single-scattering-albedo** $\omega = \frac{\kappa_s}{\kappa_{ex}}$ and the **optical-depth** $\tau = h \, \kappa_{ex}$ that describe the averaged properties of a uniformly distributed layer with a height h. The resulting representation of the backscatter-coefficient σ_0 can then be expressed as a power-series in κ_s, where each term represents the return-signal with respect to an increasing number of scattering events:

$$\sigma^0 = \sigma^0_{\text{bare-soil}} \, e^{-\frac{2\tau}{\cos(\theta)}} + \sigma^0_{\text{vegetation}} + \sigma^0_{\mathcal{O}(\kappa_s) \text{ interactions}} + \cdots \quad (1)$$

In general, the response of a (bare) soil surface can be described via a "Bidirectional Reflectance Distribution Function" ($BRDF$), which represents both the magnitude and the directionality of the scattered radiation (Nicodemus et al., 1992). For the vegetation, the directionality is similarly described via the "volume-scattering phase-function" ($\hat{p}$) whereas the magnitude of the scattering-response is governed by the single-scattering albedo ω. The general form of RT1 is then given by Quast and Wagner (2016):

$$\sigma^0 = 4\pi \cos(\theta_0) \Big[f_{bs} \cos(\theta_0) BRDF(\ldots) +$$
$$(1 - f_{bs}) \Big\{ e^{-\frac{2\tau}{\cos(\theta_0)}} \cos(\theta_0) BRDF(\ldots) + \frac{\omega}{2} \left(1 - e^{-\frac{2\tau}{\cos(\theta_0)}} \right) \hat{p}(\ldots) + \sigma^0_{int} \Big\} \Big]$$
$$(2)$$

where the parameter f_{bs} accounts for the fraction of bare-soil within the observed area and the term σ^0_{int} depicts all first-order (e.g. double-bounce) interaction contributions (represented as half-space integrals over the product of $\hat{p}$ and the $BRDF$).

In order to fully specify the RT1 model, both $\hat{p}$ and the $BRDF$ as well as the effective vegetation parameters ω and τ have to be parameterized via functional representations that relate the general radiative-transfer descriptors to biophysical variables such as soil moisture, vegetation-water-content, roughness, etc... The complexity of these parametrizations however has to be specified in accordance to the characteristics of the datasets under investigation in order to avoid the problem of under-determination within the retrieval procedures. Finding an adequate trade-off between a physically meaningful representation of the observed scene and a computationally suitable representation, whose functional complexity is simple enough to allow unambiguous evaluation of unknown parameters, is therefore a key task for the parametrization of the RT1 model.

2.2. RT1 model parametrization

In the following, a summary of the parametrization strategy used within the presented study is given. A discussion of the implications and influencing factors that led to the selected parametrizations is given in Section 3.4.1.

2.2.1. Bare soil

Many semi-empirical bare soil scattering models exist in literature that focus just on the parametrization of the mono-static (e.g. back-scattering) component of the scattered radiation via a combination of statistical roughness parameters (correlation-length λ, root-mean-square-height $RMSH$) and Fresnel-reflection coefficients (Oh, 2004; Dubois et al., 1995; Baghdadi and Zribi, 2006; Fieuzal and Baup, 2016). However, in order to estimate the strength of first-order interaction-contributions (σ^0_{int} in Eq. (2)), it is necessary to parameterize the full bistatic scattering characteristics. In theory, a description of electromagnetic scattering from a rough surface can be obtained via the so-called Integral Equation Model (IEM/IEMM Álvarez-Pérez, 2001) or one of its successors IEM2M (Álvarez-Pérez, 2012), AIEM (Chen et al., 2015). While IEM calculations provide valuable insights in the general scattering mechanisms, an optimization of the required model parameters via a non-linear regression in conjunction with a dynamic vegetation-correction on a large database is not computationally feasible. Since the presented study aims to provide a scalable parametrization, applicable for big-data processing, the complexity in modeling the soil scattering behavior is greatly reduced by using a generalized Henyey–Greenstein function (Eq. (3)) as introduced in Quast et al. (2019). This function represents a peak in specular direction

that is normalized with respect to the nadir ($\theta_0 = 0$) hemispherical reflectance (N). The width of the peak can be adjusted via the directionality-parameter t (0 for a Lambertian surface, 1 for a mirror) and the parameter a allows introducing an anisotropy in the incidence-angle behavior. This definition allows to disentangle the parameters (t, a) that govern the incidence-angle behavior of the BRDF (related to soil roughness, texture etc.) from the parameter N that sets the overall magnitude of the scattered radiation (related to the soil-permittivity ϵ and consequently, in the microwave-domain, to soil moisture).

$$BRDF(N, t, a) = \frac{N}{R_0(t,a)} HG(t, \tilde{\Theta}_a) \quad \text{with} \quad (3)$$

$$HG(t, \Theta) = \frac{1}{4\pi} \frac{1 - t^2}{\left[1 + t^2 - 2t\cos(\Theta)\right]^{3/2}}$$

$$\tilde{\Theta}_a = a\cos(\theta_0)\cos(\theta_s) - \sin(\theta_0)\sin(\theta_s)\cos(\phi_0 - \phi_s)$$

$$R_0(t, a) = \frac{(1 - t^2)}{2a^2 t^2}\left[\frac{(1 + t^2 + at) - \sqrt{(1 + t^2 + 2at)(1 + t^2)}}{\sqrt{(1 + t^2 + 2at)}}\right]$$

(θ_0, ϕ_0) and (θ_s, ϕ_s) hereby represent the direction of the incident- and scattered radiation.

Note that this parametrization avoids introducing a direct relationship to (geometrically defined) statistical roughness parameters (λ, $RMSH$) but rather aims to be a more generic description of the bistatic scattering distribution resulting from wave–particle interactions in the first few centimeters of the soil. The effects of soil properties on the microwave backscattering coefficient $\sigma^0(\theta, \phi)$ are therefore effectively represented via the scattering directionality parameter t and its numerical value is optimized within the retrieval procedure.

2.2.2. Vegetation

The ability of the vegetation-layer to scatter or absorb incoming radiation is described via the radiative-transfer parameters **single-scattering-albedo** ω and **optical-depth** τ. Furthermore, the angular scattering-distribution of the vegetation-layer is parameterized via a so-called "volume scattering phase-function" $\hat{p}$. In theory the shape of $\hat{p}$ could be evaluated via statistical electrodynamics, approximating vegetation constituents (e.g. trunks, leaves etc.) as simplified dielectric shapes (de Matthaeis and Lang, 2005). However, considering the properties of the utilized dataset within the presented study, an unambiguous retrieval of a large set of parameters governing the incidence-angle dependency of the vegetation-contribution to $\sigma^0(\theta)$ is not directly possible. With only one incidence-angle per measurement, the directionality of $\hat{p}$ and the single-scattering albedo ω are ambiguous parameters with respect to the zero-order vegetation-contribution in Eq. (2). They could only be disentangled by studying their effects on higher-order (e.g. interaction) contributions or using bi-static measurements. Those "first-order corrections" however represent only a minor contribution to the total backscatter measurement and they are similarly dependent on the used parametrization of the BRDF. Consequently, for mono-static measurements with a narrow range of incidence-angles, it is virtually impossible to perform an unambiguous retrieval of vegetation-directionality parameters alongside an estimate for ω. Therefore, the vegetation-scattering phase-function $\hat{p}$ was chosen to be isotropic.

$$\hat{p}(\Theta) = \frac{1}{4\pi} \quad (4)$$

It is important to notice that this choice for $\hat{p}$ will affect the overall magnitude of the obtained ω estimates since the zero-order vegetation-contribution is governed by the factor $\frac{\omega}{2}\hat{p}(...)$. A comparison of ω values from similar studies must therefore always be done with respect to the associated choice for $\hat{p}$. In order to incorporate the seasonal variability of the vegetation coverage, the temporal behavior of the optical depth τ is prescribed via auxiliary Leaf-Area-Index (LAI) timeseries provided by the ERA5-Land Service (2019) reanalysis dataset. While in general we expect a complex functional relationship between τ and

LAI, depending on multiple plant-physiological factors, unambiguous parametrization of such a relationship at an effective spatial resolution of 1 km is challenging and it would require extensive knowledge on the vegetation characteristics at the time of observation.

For the sake of this study, we therefore use a extremely simplified relationship by assuming a homogeneous dynamic range throughout the study-area:

$$\tau = LAI \rightarrow \text{scaled to} \in [0, 0.5] \quad (5)$$

The numerical range was chosen to preclude saturation of the absorption from the vegetation-layer, taking into account the fact that at a spatial resolution of ~1 km we always expect a fraction of the pixel to exhibit no or only moderate vegetation cover. In general, the use of auxiliary datasets inevitably adds additional uncertainties to the retrieval procedure that propagate to the obtained model parameters. Large differences in magnitude that are not reflected in the σ^0 measurements as well as instantaneous "jumps" or gaps in the data will complicate the retrieval procedure and consequently degrade the soil moisture retrieval performance. The utilized ERA5-Land dataset has an effective spatial resolution of ~9 km that represents the monthly climatology obtained from the MODIS MOD12A2 LAI product (ECMWF, 2018). As such it represents a continuous, generally "well-behaved" timeseries that can directly be used to approximate the expected seasonal dynamics of the vegetation-cover. The spatial variability of the LAI dataset however is insufficient to capture abrupt changes in the magnitude of the σ^0 vegetation contribution at 500 m sampling. The spatial dynamics of the LAI dataset were therefore harmonized to avoid issues with the spatial representativeness of the LAI dataset, and the retrieved ω values consequently subsume all remaining spatial variability of the vegetation-cover within the RT1 parametrization.

2.3. Retrieval procedure

The retrieval procedure is based on a non-linear least squares regression utilizing the trust-region-reflective Levenberg–Marquardt algorithm (Moré, 1978) as implemented in the python module `scipy.optimize` (Virtanen et al., 2020). The optimization minimizes the root mean square difference between the observed and modeled backscattering-coefficient of the whole timeseries $\Delta\sigma = \sqrt{\sum(\sigma^0_{observed} - \sigma^0_{modelled})^2}$ for each pixel individually. $\sigma^0_{modelled}$ is calculated via Eq. (2), and the parametrization of the remaining unknown parameters ω, t and N is done as follows:

Since the moisture state of the soil surface can change completely from one timestamp to the next, a unique N value is optimized for each Sentinel-1 timestamp. As stated in Quast et al. (2019), physical plausibility considerations (based on Kirchhoff's law and measurements on C-band emissivity) suggest $N < 0.1$. The range of N within the retrievals has therefore been chosen between [0.01, 0.075] with a start-value of 0.025. The actual bare-soil scattering response $\sigma^0_{bare\_soil}$ is determined by both N and the accompanying directionality parameter t_s of the BRDF-function (as defined in Eq. (3)). This parameter was estimated for each pixel as a temporally constant parameter within a range of [0.01, 0.5] and a start-value of 0.2. t_s hereby fully specifies the bistatic soil scattering directionality which is required for the estimation of first-order interaction contributions. It is important to note, that since we are dealing with mono-static measurements with a narrow range of incidence-angles, the bistatic part of the distribution must be seen as a "best-guess" and not as a reliable estimate (which could only be obtained when using an actual bistatic measurement configuration). Finally, a unique (temporally constant) ω value is optimized for all timestamps that belong to a given Sentinel-1 orbit ID. This is done to account for systematic differences with respect to changing azimuth and incidence-angles. Depending on the Sentinel-1 orbit-coverage pattern (Fig. 4), this leads to 2–4 individual ω values per pixel. The range of possible values is set to [0.01, 0.5]. Since ω represents the primary parameter that governs the strength of the

Table 1
Summary of the parameter specifications used in the presented results.

	Min	Max	Start value	Frequency
N	0.01	0.075	0.025	Per observation
ω	0.01	0.5	[0.05, 0.25, 0.4]	Per orbit
t_s	0.01	0.5	0.2	Constant

vegetation-contribution, a set of 3 different start-values (0.05, 0.25 and 0.4) have been processed to assess the impact of different start-values on the obtained parameter-estimates (see Table 1).

2.4. Urban area, water-body and topography masking

Urban areas and water-bodies are masked using the resampled CCI land cover classification as described in Section 3.2. To avoid considering pixels that show physical properties that contradict certain model assumptions (e.g. snow-cover, frozen-soil or areas with high topographic complexity) a topography mask is incorporated. Threshold values for masking are defined with respect to the mean (h_{mean}) and standard-deviation (h_{std}) of the orthographic height within a 500 m × 500 m pixel based on the 90 m Copernicus Digital Evaluation Product (Fahrland, 2020). For the presented study, any point that exhibits $h_{mean} > 675$m or $h_{std} > 35$m is masked. This masking results in a number of ~165000 valid and ~135000 masked pixels. The resulting mask is visible in Fig. 3.

3. Datasets

3.1. Study area

The study region is the catchment area of the Po river in Northern Italy with some smaller contributing areas in Switzerland. It is the largest basin in Italy, covering ~24% of the Italian national territory with a population of ~17 million inhabitants, contributing ~ 38% of the national GDP (~35% of the national agricultural product) (Mosello, 2015). The climate (classified via the Köppen climate classification Kottek et al., 2006) ranges from "humid subtropical" to "hot-summer mediterranean". Annual precipitation is ~ 1200 mm and monthly mean temperatures range from 0–5 °C in winter (January) to 22–25°C in summer (July). The North-Western part of the basin is covered by the Alps with barren mountains ranging above 4000 m whereas the central flat basin (referred to as the "Po-valley") is dominated by agricultural areas used for intensive cultivation of rice, grapes, cereals, vegetables and fruits. The selected area covers ~75000 km^2, encompassing more than 300000 pixels at the used spatial sampling of 500 m. (See Fig. 1).

3.2. CCI land cover

The European Space Agency (ESA) CCI land cover dataset v2.0.7 (European Space Agency (ESA), 2017) at 300 m spatial resolution is used to assess the retrieval performance (Section 4) for different land cover classes. The dataset is aggregated from the initial grid (equidistant Latitude–Longitude grid with 0.002778 degree separation) to the spatial sampling used within this study (500 m Equi7EU grid BM et al., 2019) by assigning the most commonly encountered land cover class among the intersected pixels (on average, each 500 m pixel is intersected by ~ 4 CCI landcover pixels). The resulting classification is shown in Fig. 2

Fig. 1. Location of the study area (Background map: Sentinel-1 global backscatter model (vv) Bauer-Marschallinger et al., 2021a).
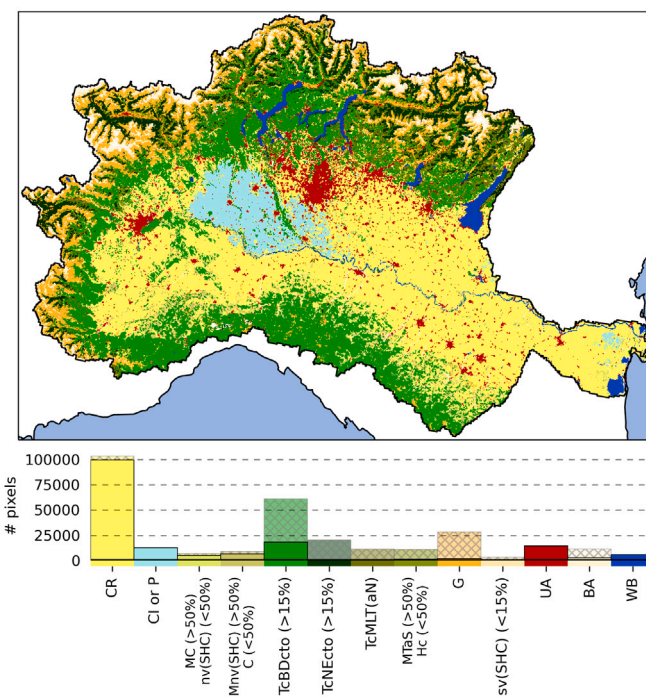

Fig. 2. CCI landcover classification with respect to the most commonly encountered landcover-class for each 500 m pixel. The used abbreviations are specified in Appendix.

3.3. Copernicus global digital evaluation model (CopDEM)

Topographic information is obtained from orthometric height mosaics based on the global 90 m Copernicus Digital Evaluation Model (CopDEM). Fahrland (2020) The dataset is further aggregated (in the same way as the CCI Land Cover) to the 500 m Equi7 grid, and the corresponding mean and standard-deviation of the orthometric heights of the intersected pixels are evaluated. (For the area of interest, each 500 m pixel is covered by ~ 40 CopDEM pixels) The resulting topography is indicated in Fig. 3

3.4. Sentinel-1

Observational input to our RT1 soil moisture retrieval is generated by the C-band sensor (CSAR) onboard the Sentinel-1 A and -1B satellites
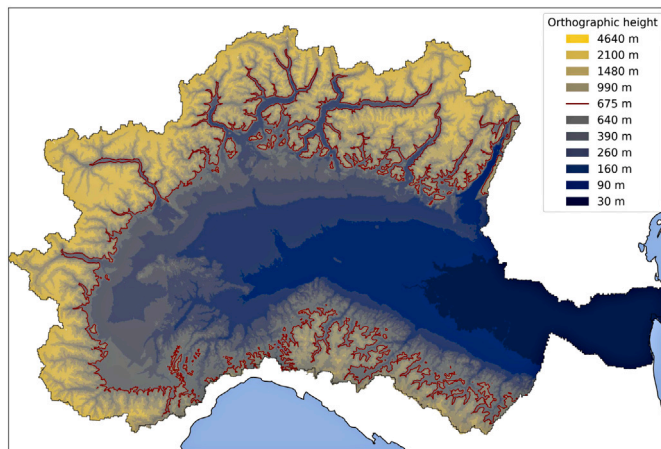
Fig. 3. Mean CopDEM orthographic height resampled to the 500 m Equi7 grid.

Fig. 4. Number of unique Sentinel-1 orbits available per pixel for the selected study-period. Masked pixels are indicated with a dimmed color. Both histogram and legend depict only pixels that are not masked. (For interpretation of the references to color in this figure legend, the reader is referred to the web version of this article.)

of the European Copernicus program, operated in the Interferometric Wide-swath (IW) mode that is the mission's main operational mode over land and measures backscatter in dual-polarization (VV and VH). In IW mode, Sentinel-1 offers a systematic and regular revisit of 9 to 1 local observations within 12 days, following the mission's orbit cycle and its observation scenario[1] (see details in Bauer-Marschallinger et al., 2019, 2021b). In the Po-Valley in northern Italy the ground coverage leads to one observation every 1–5 days. Over our study region, we collected for the period 2016–2019 all available Ground-Range-Detected at High resolution (GRDH) data at VV-polarization. This data holds backscatter amplitudes and is specified by a 10 m pixel spacing, a nominal spatial resolution of 20 m × 22 m, and a radiometric accuracy of 1 dB (3σ) (Torres et al., 2012). All products underwent preprocessing (Wagner et al., 2021) with our dedicated python package s1_sigma, embedding workflows for image- and signal-processing, and a parallelized SAR-preprocessing module environing the Sentinel-1 Toolbox[2] (S1TBX) of ESA's Sentinel Application Platform (SNAP v7.0). For each IWGRDH file we subsequently applied 1) orbital state vectors, 2) image border noise removal (following an algorithm developed specifically for S-1 Ali et al., 2018), 3) annotated radiometric calibration factors, 4) slant range – zero Doppler geometric terrain correction (using a combined 3arcsec SRTM/GDEM elevation model [VFP SRTM DEM at 90 m pixel sampling (de Ferranti, 2015)]), yielding an intermediate image at 10 m pixel sampling in geographical coordinates. Using gdalwarp,[3] each file is projected onto the Equi7Grid (Bauer-Marschallinger et al., 2014) and downsampled with Gaussian filtering to a 500 m pixel-size, and split into 600 km-sized tiles (following the approach of Bauer-Marschallinger et al. (2019)). The obtained Sentinel-1 backscatter images hold σ^0_{VV} (VV-polarized sigma nought) backscatter coefficient values in decibel (dB). More details on the applied SAR preprocessing can be found in Naeimi et al. (2016), Elefante et al. (2016), Ali et al. (2018) and in the specifications for the Sentinel-1 DataCube (Wagner et al., 2021).

3.4.1. Implications of the data characteristics

A discussion of the utilized methodologies and the obtained results can only be done in conjunction with the characteristics of the used radar-dataset as well as the incorporated auxiliary datasets. Properties such as the spatial/temporal/radiometric resolution or the observation geometry will act as limiting factors in the search for suitable soil-
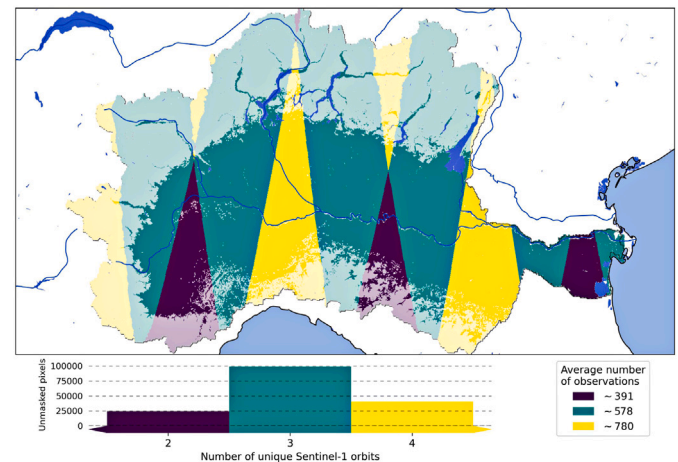
and vegetation parametrizations and impact the performance of the retrieval procedure and the interpretation of the obtained validation metrics. The following section therefore summarizes important aspects of the Sentinel-1 σ^0 data characteristics and their implications on the presented study.

Spatial resolution. In order to reduce noise and speckle effects, the Sentinel-1 data is re-sampled to an effective spatial resolution of ∼1 km (500 m spatial sampling) prior to soil moisture retrieval. An image's pixel of 1 km × 1 km encompasses several different soil- and vegetation characteristics within its area. The obtained parameters consequently serve as an spatial average that effectively represents the combined radar response.

The initial re-sampling from the native sampling of Sentinel-1 (∼10 m) to the 500 m pixel spacing aims to enhance the soil moisture retrieval's robustness, recognizing the high SAR signal complexity at the 10 m scale. Additionally, extremely high backscatter values originating from corner-reflectors, as well as extremely low values from water-bodies, have been dynamically masked prior to the re-sampling process. The retrievals are therefore expected to show a noticeable soil moisture response even in populated areas. This sensitivity however must be seen as an extrapolation of measurements from surrounding soil moisture sensitive areas.

Temporal resolution and coverage pattern. The satellites of the Sentinel-1-constellation (S1A and S1B) operate in a near-polar sun-synchronous orbit with a 12 day repeat cycle and 175 relative orbits per cycle (Torres et al., 2012).

As can be seen in Fig. 4, the implemented mission observation scenario[4] creates an inhomogeneous number of unique orbits that cover a given pixel. This pattern leads to a variable number of measurements (= inhomogeneous effective temporal resolution > 1 day) depending on the number of total covering orbits (e.g. ∼390 ± 12 observations for 2 orbits, ∼580 ± 18 for 3 orbits and ∼780 ± 28 for 4 orbits, in the period 2016–2019).

Certain regions are therefore captured more often than others and both, the density of measurements as well as the time-difference between two consecutive measurements, can vary greatly. This results in the following implications:

- The inhomogeneous data-density will impact how performance-metrics such as R or RMSD compare, since they are in general dependent on the number of available observations. However since the number of observations is always bigger than 390, the resulting metrics are expected to provide a robust estimate that is barely affected by the orbit-pattern.
- The distribution of incidence-angles is dependent on the available satellite orbits. This will affect the retrieval of soil- and vegetation parameters since the separation between soil- and vegetation contributions is incidence-angle dependent. The lack of information from certain incidence-angles will make the distinction of different parameter combinations more difficult and as a consequence the selected start-values might have a greater impact on the retrieved parameter estimates.
- Individual orbits observe areas not only at different incidence-angles, but also look at the scenes from different directions (e.g. ascending/descending). This results in a periodic "orbit-bias" that is dependent on both the topography as well as the angular distribution of the physical properties of the observed scene. Since the temporal coverage is already limited, methods for correcting such orbit-effects are necessary in order to maintain the temporal resolution and to avoid a "sawtooth"-like appearance of the retrieved SM timeseries.

Landcover and topography. The density of the vegetation-cover, the presence of artificial structures as well as the steepness and topographic complexity of the terrain can have a significant impact on the usability of Sentinel-1 data for SM retrieval. Therefore, the interpretation of results for mountainous regions, dense forests or close to densely populated areas must be performed with care as the underlying σ^0 measurements might exhibit a significantly different behavior compared to sparsely vegetated areas in flat terrain.

3.5. ERA5-land

The ERA5-Land dataset is a "replay of the land component of the ERA5 climate reanalysis with a finer spatial resolution: 9 km grid spacing", providing information on soil- and vegetation variables at hourly timestamps on a global scale (Service, 2019). Within this study the following parameters have been used:

- lai_lv (Parameter ID: 66) : Leaf area index, low vegetation [m^2/m^2]
  "*This parameter is the surface area of one side of all the leaves found over an area of land for vegetation classified as 'low' (e.g. crops and mixed farming, irrigated crops, short grass, tall grass, tundra, semidesert, bogs and marshes, evergreen shrubs, deciduous shrubs, and water and land mixtures)*".
  The data is used to simulate the seasonal component of the attenuation of the signal during the propagation through the vegetation-layer. See Section 2.2 for further discussion on the actual incorporation of the LAI variability within the presented study.
- swvl1 (Parameter ID: 39: Volumetric soil water layer 1 [m^3/m^3]
  This parameter is the volume of water in soil layer 1 (0–7 cm, the surface is at 0 cm).
  The dataset is used as a reference-dataset to assess the quality of the obtained retrievals presented in Section 4.

4. Results and discussion

4.1. SM retrieval performance

The following section presents results for the selected RT1 model parametrization applied to a set of ~300000 σ^0 timeseries from 2016 to 2019, using 3 different retrieval start-values for ω, processed with and without the consideration of first-order interaction contributions. The soil moisture retrieval performance is hereby discussed by analyzing the Pearson-correlation (R) between the retrieved timeseries for N and the top-layer soil moisture estimates ("swvl1", depth = 0–7cm) provided by ERA5-Land ECMWF (2018). This analysis therefore implies a linear relationship between the nadir-hemispherical reflectance (N) and the volumetric soil moisture in the top soil-layer. In order to assess the impact of the aforementioned Sentinel-1 orbit-pattern, results are further analyzed with respect to the number of available orbits to identify possible issues that have to be addressed when dealing with Sentinel-1 derived soil moisture datasets.

Fig. 5 shows the spatial distribution of the Pearson correlation (R) for the retrieved N parameter and the ERA5-Land top-layer soil moisture variable $swvl1$ using $\omega_{start} = 0.25$ without first-order corrections. The obtained distribution indicates an overall good agreement between the variables with a mode of $R_{mode} \sim 0.6$ and a median of $R_{median} \sim 0.56$.

The retrieval procedure in general is affected by numerous influencing factors. In the following, we focus on assessing the impact of:

- different choices for the ω start-value within the retrieval
- the respective CCI landcover class for each pixel
- the number of available Sentinel-1 orbits (see Fig. 4)
- the consideration of first-order interaction contributions in the retrieval

Fig. 6 indicates the obtained R distributions resulting from the 3 different ω start-values, classified with respect to the most common landcover-types as well as the number of unique Sentinel-1 orbits. Since the individual distributions represent results from different locations (which might exhibit very different soil and vegetation characteristics), a direct comparison of the values must be performed with care. However, it is possible to deduce several general aspects of the retrieval procedure: The consideration of first-order interaction effects seem to provide only minor improvements on the soil moisture retrieval performance. Considering the properties of the available σ^0 measurements, this is however not surprising since the magnitude of these corrections is highly dependent on the bistatic scattering characteristics of soil- and vegetation and the corrections primarily affect the incidence-angle dependency of the modelled σ^0. The limited number of available incidence-angles from Sentinel-1 makes it virtually impossible to obtain the necessary information to unambiguously parameterize the model for higher order corrections. Consequently we will in the following limit the analysis to configurations that omit higher-order corrections.

A distinct feature visible in Fig. 6 that might come as a surprise is the fact that the obtained correlations are actually higher for forested areas than for "Croplands" & "Herbaceous cover".

Separating long- and sort-term trends (see Fig. 8) however reveals that this increase in correlation is solely related to the fact that the representation of the long-term soil moisture variability is much better for areas covered by natural vegetation compared to croplands. The representation of soil moisture anomalies on the other hand shows a similar performance. A detailed analysis of the individual performance of long- and short-term soil moisture variabilities is given in Section 4.1.1.

Finally, it is clearly visible that the selected start-value for ω has a much lower impact on the soil moisture retrieval performance for "Croplands" & "Herbaceous cover" than for densely vegetated areas (e.g. Tree cover) where higher start-values result in significantly higher correlations. This indicates that using start-values based on landcover-classifications might provide considerable improvements in the retrieval performance, especially over densely vegetated areas.
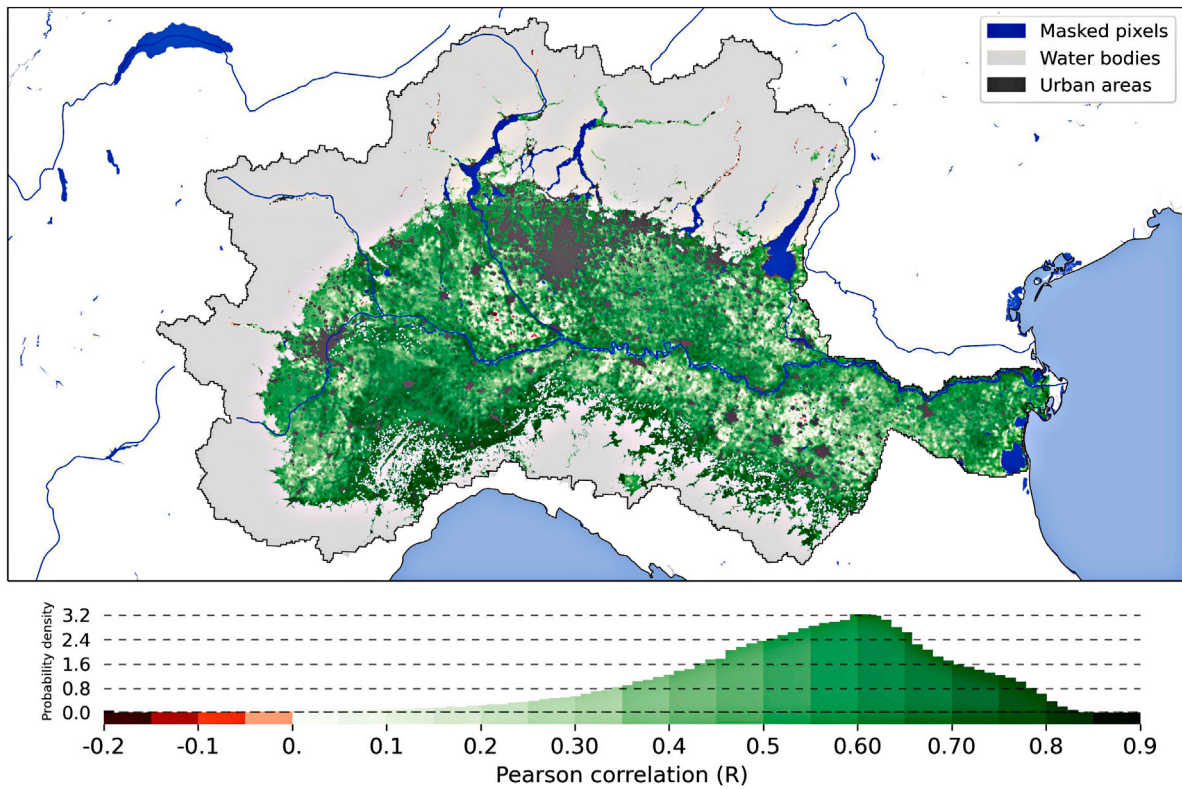
Fig. 5. Pearson-correlation (R) between RT1 N and ERA5-Land $swvl1$ for $\omega_{start} = 0.25$ without first-order corrections. Results are masked with respect to topography, and all pixels classified by the CCI landcover as "Water body" or "Urban area" are excluded.
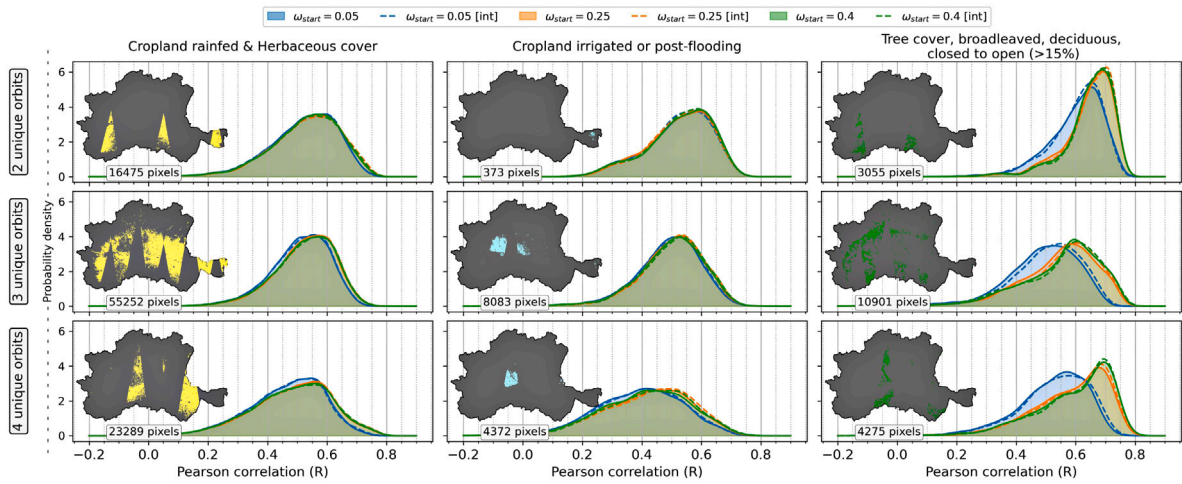

Fig. 6. Dependency of the Pearson-correlations (R) for RT1 N and ERA5-Land $swvl1$ on the used retrieval start-value for ω. Results are classified with respect to the most common CCI-Landcover classes and split with respect to the number of Sentinel-1 orbits available per pixel. The small maps indicate the location of relevant pixels. The suffix [int] indicates retrievals that consider first-order interaction contributions.

4.1.1. Soil moisture anomalies

An individual analysis of soil moisture anomalies is highly dependent on the method used for separating long- and short-term dynamics. In the following, the long-term dynamics are identified by applying a rolling-mean filter with 30, 60, 90 and 120 days to both the RT1 and the ERA5-Land soil moisture timeseries. Fig. 7 indicates the resulting Pearson correlation distributions which clearly reveals the impact of the length of the rolling mean filter. Despite the difference between the mean-value periods, we see that long-term dynamics show higher correlations with values around $R_{median} \sim 0.7$–0.8 whereas anomalies obtain $R_{median} \sim 0.5$–0.55.

Fig. 8 depicts the obtained correlations (anomalies, seasonalities and absolute-values) classified with respect to the CCI landcover for the 90 days rolling period. Looking at the anomalies, we see that rainfed croplands as well as areas covered by natural vegetation show a similar performance ($R_{median} \sim 0.55$) while "Irrigated or post-flooding croplands" exhibit a lower correlation ($R_{median} \sim 0.45$). The reason for this might be either the distinctly different scattering behavior of the intermittently flooded fields resulting in anomalous soil moisture retrievals, or it might be an indication of actual soil moisture signals originating from irrigation-practices that are present in the retrievals but not adequately represented in the ERA5-Land $swvl1$ dataset.
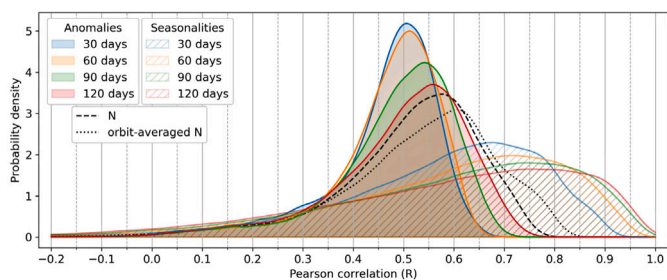
Fig. 7. Distribution of single-pixel Pearson correlations for seasonalities and anomalies of N vs. $swvl1$ with respect to different evaluation periods (for the configuration using $\omega_{start} = 0.25$). The seasonality hereby represents a rolling-mean of the respective time-period, and the anomalies represent the remaining difference between the seasonality and the actual retrievals.

Considering the long-term dynamics, we see that areas covered by natural vegetation are generally better represented than Croplands or Herbaceous cover. This is attributable to the fact that long-term soil- and vegetation dynamics are better represented for "natural" areas, whereas the spatial resolution of ~9 km of the auxiliary dataset (used to mimic the seasonal dynamics of τ) as well as the comparison-dataset (used for evaluating the soil moisture correlations) does not represent the dynamics of croplands (irrigation, tilling, harvesting etc.) in the same way as the utilized Sentinel-1 σ^0 dataset (which is affected by variabilities at an effective spatial resolution of ~1 km).

The spatial patterns of the anomaly and seasonality correlations are both similar to Fig. 5.

4.1.2. Impact of the sentinel-1 orbit pattern

Fig. 9 shows timeseries grouped with respect to the number of available Sentinel-1 orbits for forested areas and areas covered by croplands.

From the general appearance of the timeseries, we see that the overall dynamics are similarly well represented, whereas an increasing number of orbits adds a "sawtooth-like" disturbance to the soil moisture timeseries which stems from unaccounted differences of the σ^0 observations originating from different orbits. The added value of a much higher temporal resolution (from ~4.5 daily observations to ~ daily observations) therefore introduces at the same time the need for orbit-corrections. Whether it is better to perform these corrections on the σ^0 timeseries prior to the retrievals or as a post-processing step on the retrieved parameter-timeseries remains an open question that requires further analysis. Possible methods to tackle this problem include orbit-dependent mean-standard deviation scaling, cumulative distribution function (CDF) matching or timeseries based approaches like rolling averages or Savitzky–Golay filters or combinations of the aforementioned methods. In general, it is important to devise methods that correct only for systematic effects introduced by the orbits (e.g. observation-geometry and time etc.) while maintaining the actual signal variabilities introduced by soil- and vegetation dynamics between consecutive measurements.

4.1.3. In situ comparison

In the following, a comparison with respect to all available in situ network provided by the International Soil Moisture Network (ISMN) (Dorigo et al., 2021) is given.

It must be noted that this analysis is only provided for completeness since the available data is not sufficient do draw definite conclusions.

Results for the 2 available networks are shown in Fig. 10. The UMSUOL network (Pasquali, 2023) provides a single sensor located in flat, primarily agricultural area at a depth of 10 cm. Despite the short time span (until March 2017), the comparison indicates an overall good agreement to the RT1 retrievals.

The second network (STEMS (Darouich et al., 2022), 4 sensors at 10 cm depth) is part of a long-term soil erosion experiment, aiming to evaluate effects of agricultural management practices on the hydrologic, soil erosion and soil compaction process in vineyards. All 4 sensors are encompassed within a single 500 m pixel which exhibits a complex topography and a high landcover variability. These conditions are not ideal for comparison with satellite data at an effective spatial resolution of 1 km which is also evident from the high variability between the individual station timeseries. The poor agreement between the RT1 retrievals and the in situ timeseries is consequently related to the high sub-pixel variabilities that cannot be resolved at an effective spatial resolution of 1 km.

4.2. Model parameter evaluation

The retrieved temporally static model parameters (e.g. ω and t_s) provide additional insights in aspects that affect the observed Sentinel-1 σ^0 measurements and consequently the associated performance of the RT1 retrievals. Fig. 11 shows the spatial distribution of the single-scattering albedo (ω) (averaged over the Sentinel-1 orbits) as obtained when using a start-value of $\omega_{start} = 0.25$. It is immediately evident that urban areas are characterized by very high ω values. This stems from the fact that the mean σ^0 is much higher (independent of the incidence-angle range) due to the presence of strong reflection surfaces (rooftops, corner-reflectors etc.). The retrieval algorithm will react to this incidence-angle independent increase in the mean σ^0 by increasing the magnitude of the vegetation-contribution (since it represents a nearly incidence-angle independent contribution to the total simulated σ^0). Since ω is the only free parameter, acting as a multiplicative factor of $\sigma^0_{vegetation}$, densely populated urban areas exhibit very high ω values. On the other hand, large man-made structures with a comparably large fraction of bituminized or moderately vegetated areas (such as airports) show a distinctly lower ω. For example, the "Milan Malpensa Airport" as well as the 2 neighboring airports "Ghedi Air Base" and "Brescia Airport" are clearly visible in Fig. 11 (as extended areas with $\omega \sim 0.1$).

To analyze the characteristics of ω with respect to different vegetation-types, Fig. 12 indicates the distribution of the (orbit-averaged) ω retrievals for each pixel, classified with respect to the most common CCI landcover classes. The general trend again follows the a-priori expectations that croplands obtain a much lower ω than more densely vegetated areas (e.g. Mosaic cropland/natural vegetation and areas covered by broadleaved forests). Also we see that selecting an appropriate start-value for ω has a much greater impact for densely vegetated areas than croplands.

This can be explained by considering the fact that areas covered by dense vegetation show much lower dynamics in the σ^0 timeseries. This results in an increased number of possible parameter-combinations that adequately represent the observed σ^0 timeseries. The selected start-value will therefore have a stronger impact on which combination of parameters will be identified first. Looking at the associated soil moisture correlations for the forested areas (Fig. 6), we see that while the model is capable of representing the observed σ timeseries also with a lower single-scattering albedo (e.g. using $\omega_{start} = 0.05$), a comparison of the resulting soil moisture timeseries to ERA5-Land shows a much lower correlations. For croplands on the other hand, a high consistency between the different start-values is found. This indicates that despite the overall under-determination of the retrieval procedure, the regressand (e.g. $\sum (\sigma^0_{observed} - \sigma^0_{modelled})^2$) shows a clear minimum with respect to the obtained distribution of ω values for moderately vegetated areas.

The spatial distribution of the soil scattering-directionality parameter (t_s) is depicted in Fig. 13. In the same way as before, the most prominent features are airports which seem to show a distinctly different behavior than other (sufficiently large) man-made structures. This time, they exhibit a unusually high t_s compared to other areas. In general, a higher t_s (effectively representing a "smoother" surface) represents a steeper decrease of the (bare-soil) σ^0 with increasing
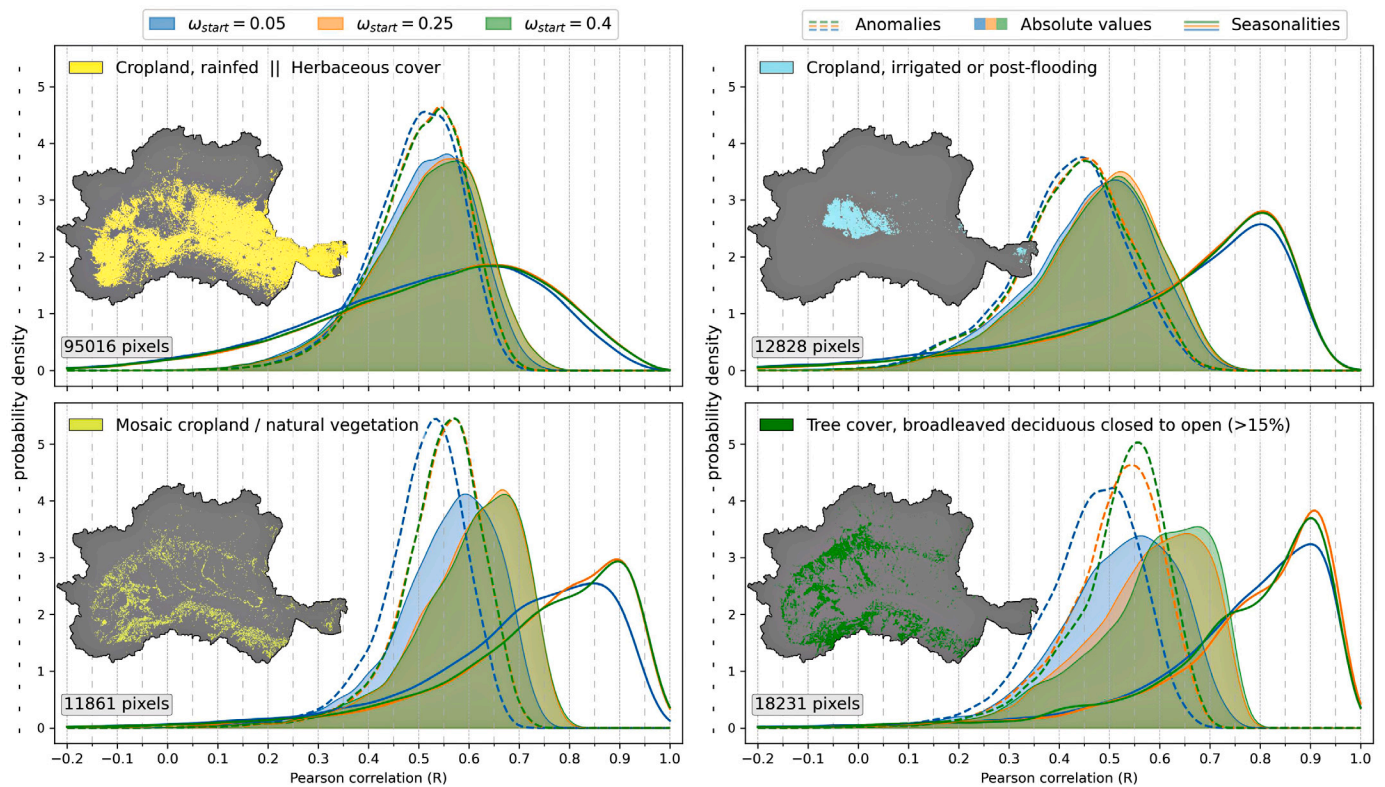
Fig. 8. Single-pixel Pearson-correlations for seasonalities and anomalies calculated with respect to a 90 day rolling mean, classified with respect to the most commonly encountered CCI landcover classes. Results are masked with respect to topography. The small maps indicate the location of the relevant pixels.

incidence-angle. Looking at the overall distribution of values, most areas obtain $t_s \approx 0.01$ which can again be accounted to the limited availability of incidence-angles that would be required to distinguish subtle differences in the scattering-behavior with respect to the soil-scattering directionality. The obtained value-range ($0.01 < t_s < 0.1$) hereby represents only minor corrections to the calculated σ^0 compared to the impact of other optimized parameters (e.g. N and ω).

Despite the limitations involved in obtaining a representative estimate for t_s, a classification with respect to the CCI Landcover (Fig. 14) still reveals a clear difference between natural and agricultural areas. A considerable fraction of areas covered by natural vegetation hereby shows a distinctly higher t_s compared to croplands, which are nearly everywhere represented by $t_s = 0.01$.

5. Conclusion

The presented study represents a first assessment of the applicability of the RT1 modeling framework for retrieval of high-resolution (~1 km) soil moisture from Sentinel-1 SAR C-band backscatter measurements. Important aspects concerning the use of high-resolution Sentinel-1 data are highlighted and a thorough analysis of the performance of the obtained retrieval performance for a set of ~ 300000 pixels over a 4-year time-period from 2016 to 2019 is given. The overall good correlations with respect to the ERA5-Land top-layer soil moisture variable ($swvl1$) (median Pearson correlation of 0.6) highlights the potential of using resampled Sentinel-1 SAR σ^0 measurements for the generation of high-resolution soil moisture datasets. The utilized radiative transfer based model (RT1) hereby serves as a flexible and extensible method that performs well under a variety of different landcover types and data-characteristics. To correct for effects induced by the seasonal variability of the covering vegetation layer, the utilized parametrization uses auxiliary Leaf Area Index (LAI) timeseries with magnitudes scaled to a unified range to mimic the temporal signal of the associated vegetation optical depth (τ). The spatial variability of the vegetation coverage was

then accounted for by retrieving a temporally constant single-scattering albedo (ω) estimate. The assumption of a unified dynamic range of τ together with a spatially varying ω turned out to provide a robust method for correcting long-term vegetation dynamics with a minimal number of unknown variables. While the presented parametrization provides an overall good performance over the selected study-area, future studies have to assess the applicability of the approach for large-scale processing as well as possibilities for improving the parametrization of the vegetation-correction with respect to the temporal dynamics as well as the spatial representability (e.g. by using actual high-resolution datasets to better capture the small-scale variability of the vegetation coverage). The usability of the obtained soil-moisture retrievals for the evaluation of accumulated rainfall via the SM2RAIN algorithm has been assessed by Filippucci et al. (2021), and a broader perspective on potential applications of Sentinel-1 high-resolution soil moisture retrievals for hydrological modeling is given by Alfieri et al. (2021).

CRediT authorship contribution statement

Raphael Quast: Conceptualization, Methodology, Software, Validation, Formal analysis, Investigation, Visualization, Writing – original draft. **Wolfgang Wagner:** Conceptualization, Methodology, Writing – review & editing, Supervision. **Bernhard Bauer-Marschallinger:** Data curation, Writing – review & editing. **Mariette Vreugdenhil:** Writing – review & editing, Supervision.
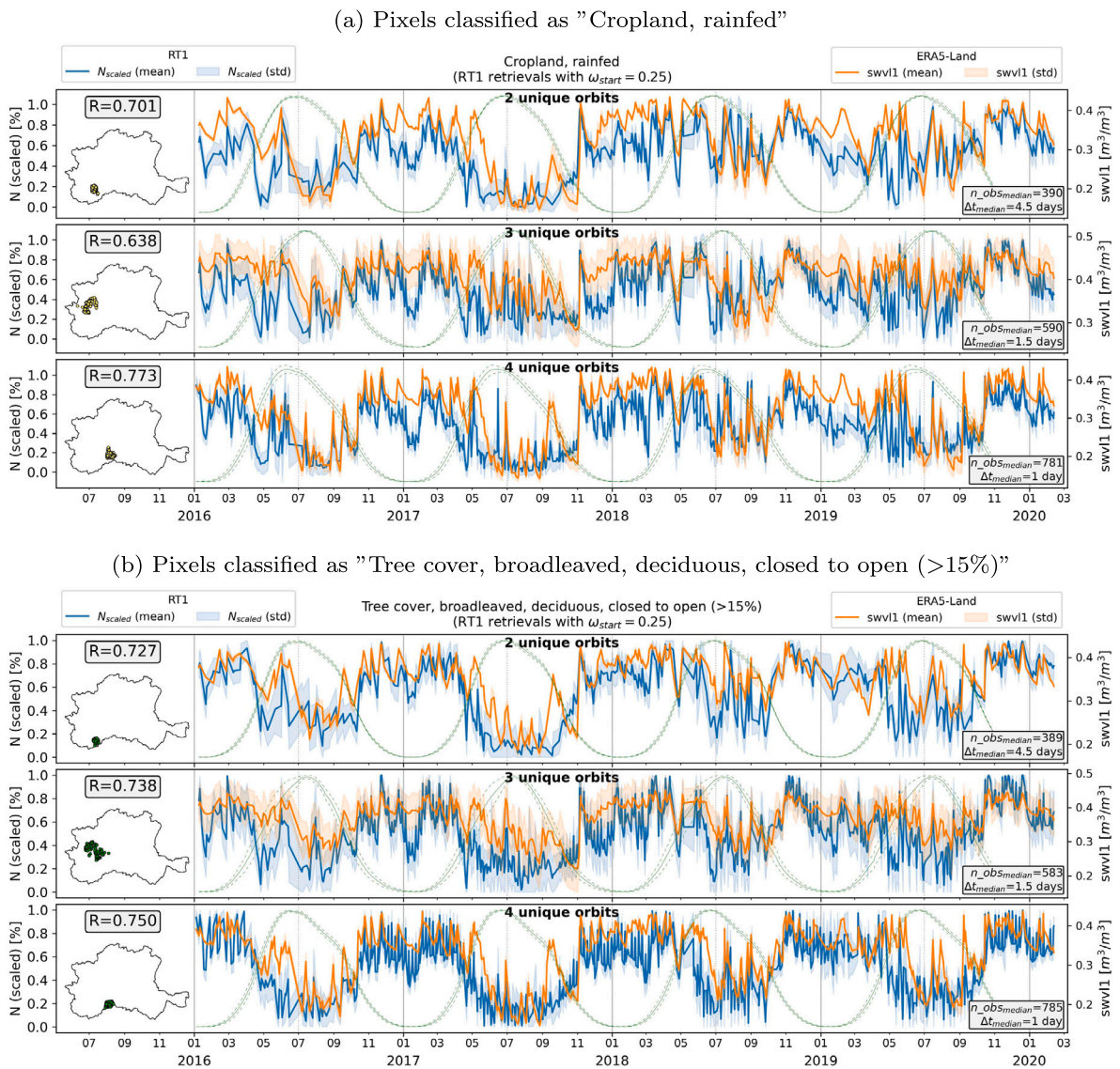
(a) Pixels classified as "Cropland, rainfed"

(b) Pixels classified as "Tree cover, broadleaved, deciduous, closed to open (>15%)"

Fig. 9. Comparison of averaged soil moisture timeseries for 100 randomly selected (clustered) pixels selected from areas classified by the same CCI landcover-class and the same number of unique Sentinel-1 orbits. The green lines indicate the mean ± standard deviation of the temporal variability of τ. (For interpretation of the references to color in this figure legend, the reader is referred to the web version of this article.)
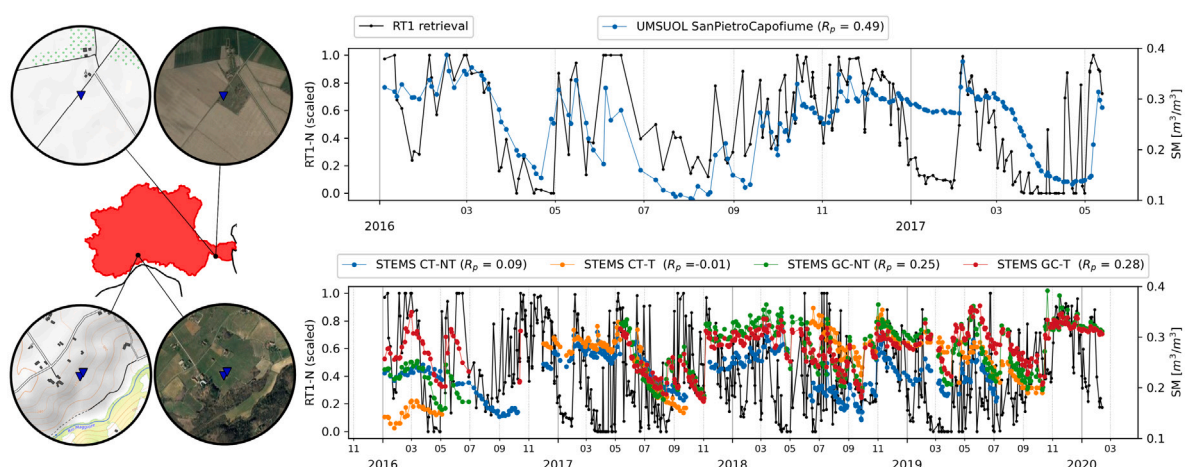
Fig. 10. In situ comparisons with respect to the available stations provided by the ISMN. The inset-maps show circular areas with 500 m radius around the stations (blue triangles). The poor agreement to the STEMS network is related to the fact that all stations are located on a hillslope and highly affected by agricultural management practices.
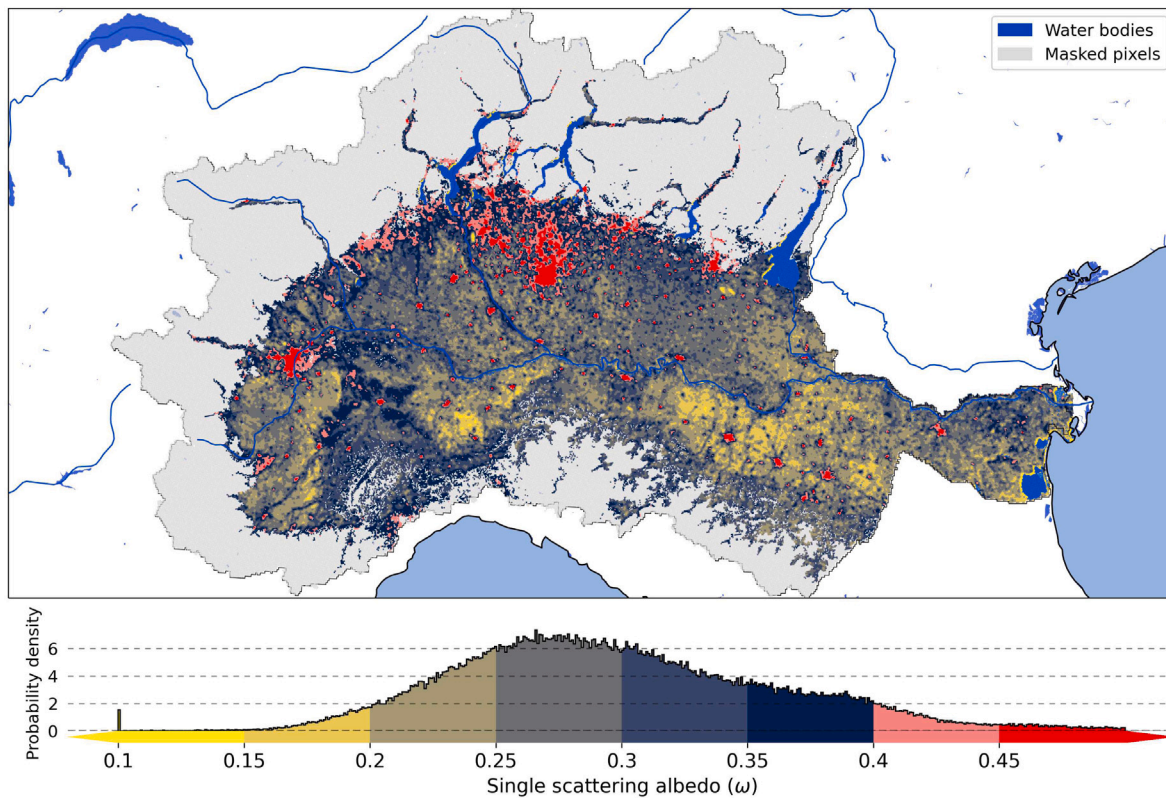
Fig. 11. Retrieved (orbit-averaged) single scattering albedo (ω) for $\omega_{start} = 0.25$. Results are masked with respect to topography and all pixels classified by the CCI landcover as "water-body" are excluded.
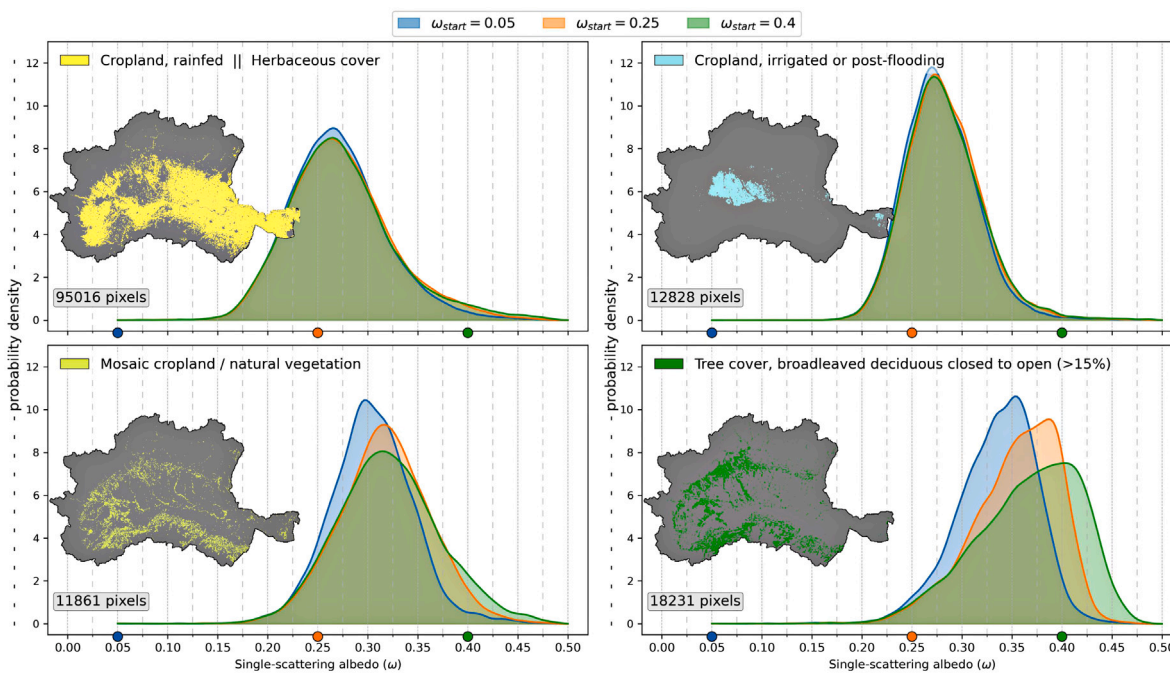

Fig. 12. Mean single scattering albedo (ω) retrievals classified with respect to the most common CCI-Landcover classes. Results are masked with respect to topography. The small maps indicate the location of relevant pixels.
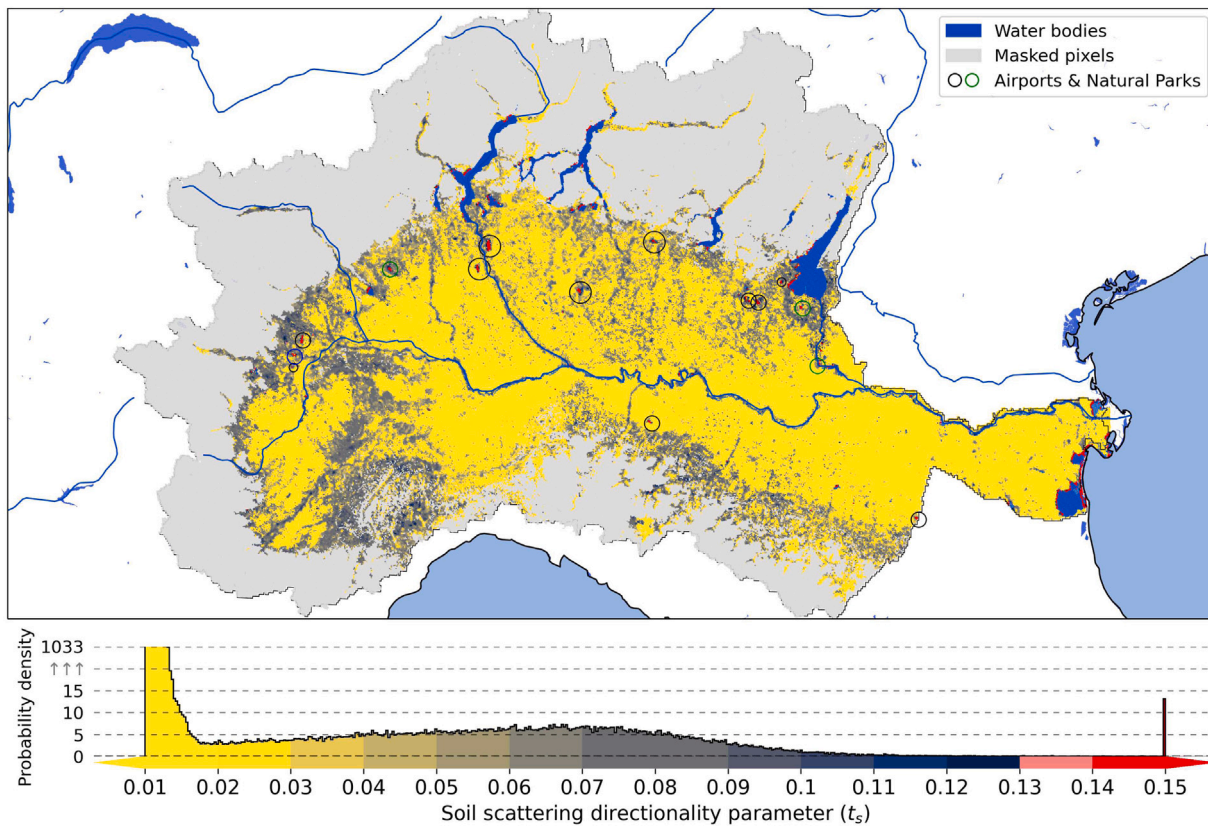
Fig. 13. Retrieved soil directionality parameter (t_s) for the best configuration that yields the best soil moisture performance. Results are masked with respect to topography and all pixels classified by the CCI landcover as "water-body" are excluded.
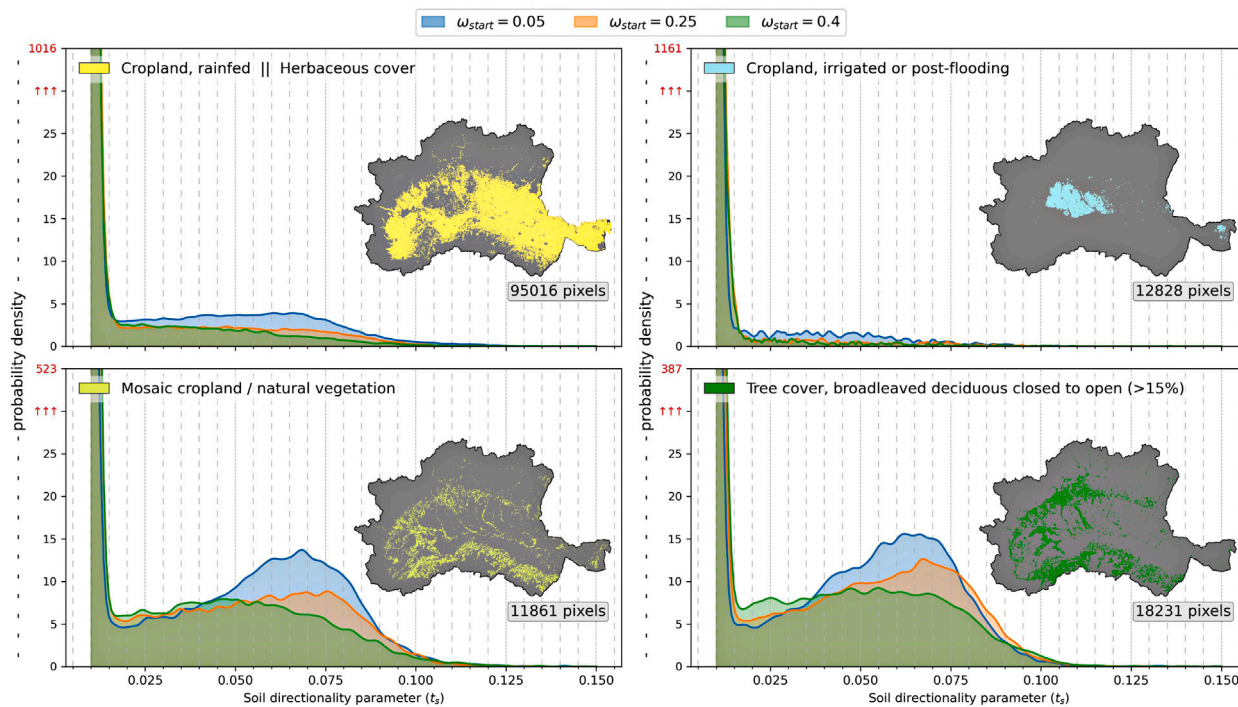

Fig. 14. Soil directionality parameter (t_s) retrievals classified with respect to the most common CCI-Landcover classes. Results are masked with respect to topography. The small maps indicate the location of relevant pixels.

Declaration of competing interest

Data availability

Data will be made available on request.

Acknowledgments

Appendix. CCI land cover legend abbreviations

Legend abbreviations as used in Fig. 2: **WB:** Waterbody, **BA:** Bare areas, **UA:** Urban areas, sv(SHC)(<15%) : Sparse vegetation (tree, shrub, herbaceous cover) (<15%), **G:** Grassland, MTaS(>50%)Hc(<50%): Mosaic tree and shrub (>50%) / herbaceous cover (<50%), **TcMLT(aN):** Tree cover, mixed leaf type (broadleaved and needleleaved, TcNEcto(>15%): Tree cover, needleleaved, evergreen, closed to open (>15%), TcBDcto(>15%): Tree cover, broadleaved, deciduous, closed to open (>15%), Mnv(SHC)(>50%)C(<50%) : Mosaic natural vegetation (tree, shrub, herbaceous cover) (>50%) / cropland (<50%), MC(>50%)nv(SHC)(>50%): Mosaic cropland (>50%) / natural vegetation (tree, shrub, herbaceous cover) (<50%), **CI or P:** Cropland, irrigated or post-flooding, **CR:** Cropland, rainfed,

References

Alfieri, L., Avanzi, F., Delogu, F., Gabellani, S., Bruno, G., Campo, L., Libertino, A., Massari, C., Tarpanelli, A., Rains, D., Miralles, D.G., Quast, R., Vreugdenhil, M., Wu, H., Brocca, L., 2021. High Resolution Satellite Products Improve Hydrological Modeling in Northern Italy. Copernicus GmbH, http://dx.doi.org/10.5194/hess-2021-632.

Ali, I., Cao, S., Naeimi, V., Paulik, C., Wagner, W., 2018. Methods to remove the border noise from sentinel-1 synthetic aperture radar data: Implications and importance for time-series analysis. IEEE J. Sel. Top. Appl. Earth Obs. Remote Sens. 11 (3), 777–786. http://dx.doi.org/10.1109/jstars.2017.2787650.

Álvarez-Pérez, J.L., 2001. An extension of the IEM/IEMM surface scattering model. Waves Random Media 11 (3), 307–329. http://dx.doi.org/10.1088/0959-7174/11/3/308.

Álvarez-Pérez, J.L., 2012. The IEM2M rough-surface scattering model for complex-permittivity scattering media. Waves Random Complex Media 22 (2), 207–233. http://dx.doi.org/10.1080/17455030.2011.649147.

Attema, E., Ulaby, F.T., 1978. Vegetation modeled as a water cloud. Radio Sci. 13 (2), 357–364.

Baghdadi, N., Zribi, M., 2006. Evaluation of radar backscatter models IEM, OH and Dubois using experimental observations. Int. J. Remote Sens. 27 (18), 3831–3852. http://dx.doi.org/10.1080/01431160600658123.

Balenzano, A., Mattia, F., Satalino, G., Lovergine, F.P., Palmisano, D., Peng, J., Marzahn, P., Wegmüller, U., Cartus, O., Dabrowska-Zielińska, K., Musial, J.P., Davidson, M.W.J., Pauwels, V.R.N., Cosh, M.H., McNairn, H., Johnson, J.T., Walker, J.P., Yueh, S.H., Entekhabi, D., Kerr, Y.H., Jackson, T.J., 2021. Sentinel-1 soil moisture at 1 km resolution: a validation study. Remote Sens. Environ. 263, 112554. http://dx.doi.org/10.1016/j.rse.2021.112554.

Bauer-Marschallinger, B., Cao, S., Navacchi, C., Freeman, V., Reuß, F., Geudtner, D., Rommen, B., Vega, F.C., Snoeij, P., Attema, E., Reimer, C., Wagner, W., 2021a. The Sentinel-1 Global Backscatter Model (S1GBM) - Mapping Earth's Land Surface with C-Band Microwaves. TU Wien, http://dx.doi.org/10.48436/N2D1V-GQB91.

Bauer-Marschallinger, B., Cao, S., Navacchi, C., Freeman, V., Reuß, F., Geudtner, D., Rommen, B., Vega, F.C., Snoeij, P., Attema, E., Reimer, C., Wagner, W., 2021b. The normalised sentinel-1 global backscatter model, mapping earth's land surface with C-band microwaves. Sci. Data 8 (1), http://dx.doi.org/10.1038/s41597-021-01059-7.

Bauer-Marschallinger, B., Freeman, V., Cao, S., Paulik, C., Schaufler, S., Stachl, T., Modanesi, S., Massari, C., Ciabatta, L., Brocca, L., Wagner, W., 2019. Toward global soil moisture monitoring with sentinel-1: Harnessing assets and overcoming obstacles. IEEE Trans. Geosci. Remote Sens. 57 (1), 520–539. http://dx.doi.org/10.1109/tgrs.2018.2858004.

Bauer-Marschallinger, B., Paulik, C., Hochstöger, S., Mistelbauer, T., Modanesi, S., Ciabatta, L., Massari, C., Brocca, L., Wagner, W., 2018. Soil moisture from fusion of scatterometer and SAR: Closing the scale gap with temporal filtering. Remote Sens. 10 (7), 1030. http://dx.doi.org/10.3390/rs10071030.

Bauer-Marschallinger, B., Sabel, D., Wagner, W., 2014. Optimisation of global grids for high-resolution remote sensing data. Comput. Geosci. 72, 84–93. http://dx.doi.org/10.1016/j.cageo.2014.07.005, URL: http://www.sciencedirect.com/science/article/pii/S0098300414001629.

Benninga, H.-J., van der Velde, R., Su, Z., 2019. Impacts of radiometric uncertainty and weather-related surface conditions on soil moisture retrievals with sentinel-1. Remote Sens. 11 (17), 2025. http://dx.doi.org/10.3390/rs11172025.

BM, B., Hahn, S., Schmitzer, M., Shochsto, Senmao Cao, 2019. TUW-GEO/Equi7Grid: uPdate on Image2equi7, Antimeridian Handling. Zenodo, http://dx.doi.org/10.5281/ZENODO.1048530.

Bojinski, S., Verstraete, M., Peterson, T.C., Richter, C., Simmons, A., Zemp, M., 2014. The concept of essential climate variables in support of climate research, applications, and policy. Bull. Am. Meteorol. Soc. 95 (9), 1431–1443. http://dx.doi.org/10.1175/bams-d-13-00047.1.

Chen, K.-L., Chen, K.-S., Li, Z.-L., Liu, Y., 2015. Extension and validation of an advanced integral equation model for bistatic scattering from rough surfaces. Prog. Electromagn. Res. 152, 59–76. http://dx.doi.org/10.2528/pier15011409.

Darouich, H., Ramos, T.B., Pereira, L.S., Rabino, D., Bagagiolo, G., Capello, G., Simionesei, L., Cavallo, E., Biddoccu, M., 2022. Water use and soil water balance of mediterranean vineyards under rainfed and drip irrigation management: Evapotranspiration partition and soil management modelling for resource conservation. Water 14 (4), 554. http://dx.doi.org/10.3390/w14040554.

Das, N., Entekhabi, D., Dunbar, R.S., Kim, S., Yueh, S., Colliander, A., O'Neill, P.E., Jackson, T., Jagdhuber, T., Chen, F., Crow, W.T., Walker, J., Berg, A., Bosch, D., Caldwell, T., Cosh, M., 2020. SMAP/Sentinel-1 L2 Radiometer/Radar 30-Second Scene 3 km EASE-Grid Soil Moisture, Version 3. NASA National Snow and Ice Data Center DAAC, http://dx.doi.org/10.5067/ASB0EQO2LYJV.

de Ferranti, J., 2015. Digital elevation data – with SRTM-voids filled using accurate topographic mapping. URL: http://viewfinderpanoramas.org/.

Dorigo, W., Himmelbauer, I., Aberer, D., Schremmer, L., Petrakovic, I., Zappa, L., Preimesberger, W., Xaver, A., Annor, F., Ardö, J., Baldocchi, D., Bitelli, M., Blöschl, G., Bogena, H., Brocca, L., Calvet, J.-C., Camarero, J.J., Capello, G., Choi, M., Cosh, M.C., van de Giesen, N., Hajdu, I., Ikonen, J., Jensen, K.H., Kanniah, K.D., de Kat, I., Kirchengast, G., Rai, P.K., Kyrouac, J., Larson, K., Liu, S., Loew, A., Moghaddam, M., Fernández, J.M., Bader, C.M., Morbidelli, R., Musial, J.P., Osenga, E., Palecki, M.A., Pellarin, T., Petropoulos, G.P., Pfeil, I., Powers, J., Robock, A., Rüdiger, C., Rummel, U., Strobel, M., Su, Z., Sullivan, R., Tagesson, T., Varlagin, A., Vreugdenhil, M., Walker, J., Wen, J., Wenger, F., Wigneron, J.P., Woods, M., Yang, K., Zeng, Y., Zhang, X., Zreda, M., Dietrich, S., Gruber, A., van Oevelen, P., Wagner, W., Scipal, K., Drusch, M., Sabia, R., 2021. The international soil moisture network: serving earth system science for over a decade. Hydrol. Earth Syst. Sci. 25 (11), 5749–5804. http://dx.doi.org/10.5194/hess-25-5749-2021.

Dubois, P., van Zyl, J., Engman, T., 1995. Measuring soil moisture with imaging radars. IEEE Trans. Geosci. Remote Sens. 33 (4), 915–926. http://dx.doi.org/10.1109/36.406677.

ECMWF, 2018. IFS Documentation CY45R1 - Part IV : Physical processes. ECMWF, http://dx.doi.org/10.21957/4WHWO8JW0.

Edokossi, K., Calabia, A., Jin, S., Molina, I., 2020. GNSS-Reflectometry and remote sensing of soil moisture: A review of measurement techniques, methods, and applications. Remote Sens. 12 (4), 614. http://dx.doi.org/10.3390/rs12040614.

Elefante, S., Wagner, W., Briese, C., Cao, S., Naeimi, V., 2016. High-performance computing for soil moisture estimation.

Elson, P., De Andrade, E.S., Hattersley, R., May, R., Lucas, G., Campbell, E., Dawson, A., Stephane Raynaud, Scmc72, Little, B., Donkers, K., Blay, B., 2021. SciTools/cartopy: v0.19.0.post1. Zenodo, http://dx.doi.org/10.5281/ZENODO.1182735.

Entekhabi, D., Njoku, E.G., O'Neill, P.E., Kellogg, K.H., Crow, W.T., Edelstein, W.N., Entin, J.K., Goodman, S.D., Jackson, T.J., Johnson, J., Kimball, J., Piepmeier, J.R., Koster, R.D., Martin, N., McDonald, K.C., Moghaddam, M., Moran, S., Reichle, R., Shi, J.C., Spencer, M.W., Thurman, S.W., Tsang, L., Zyl, J.V., 2010. The soil moisture active passive (SMAP) mission. Proc. IEEE 98 (5), 704–716. http://dx.doi.org/10.1109/jproc.2010.2043918.

ESA, 2022. Earth explorer 10 candidate mission harmony, ESA-EOPSM-HARM-RP-4129. p. 369.

European Environment Agency, 2020. WISE WFD Reference Spatial Datasets reported under Water Framework Directive 2016 - PUBLIC VERSION - version 1.4, Apr. 2020. URL: https://www.eea.europa.eu/data-and-maps/data/wise-wfd-spatial-3.

European Space Agency (ESA), 2017. Land cover CCI product. URL: https://maps.elie.ucl.ac.be/CCI/viewer/.

Fahrland, E., 2020. Copernicus Digital Elevation Model Product Handbook. Airbus, Available at https://spacedata.copernicus.eu/documents/20126/0/GEO1988-CopernicusDEM-SPE-002_ProductHandbook_I1.00.pdf, Version 2.1.

Fieuzal, R., Baup, F., 2016. Improvement of bare soil semi-empirical radar backscattering models (Oh and Dubois) with SAR multi-spectral satellite data (X-, C- and L-bands). Adv. Remote Sens. 05 (04), 296–314. http://dx.doi.org/10.4236/ars.2016.54023.

Filippucci, P., Brocca, L., Quast, R., Ciabatta, L., Saltalippi, C., Wagner, W., Tarpanelli, A., 2021. High Resolution (1 km) Satellite Rainfall Estimation From SM2RAIN Applied to Sentinel-1: Po River Basin as Case Study. Copernicus GmbH, http://dx.doi.org/10.5194/hess-2021-563.

Foucras, M., Zribi, M., Albergel, C., Baghdadi, N., Calvet, J.-C., Pellarin, T., 2020. Estimating 500-m resolution soil moisture using sentinel-1 and optical data synergy. Water 12 (3), 866. http://dx.doi.org/10.3390/w12030866.

Fung, A.K., 1994. Microwave Scattering and Emission Models and Their Applications. Artech House, Norwood, MA.

Gao, Q., Zribi, M., Escorihuela, M., Baghdadi, N., 2017. Synergetic use of sentinel-1 and sentinel-2 data for soil moisture mapping at 100 m resolution. Sensors 17 (9), 1966. http://dx.doi.org/10.3390/s17091966.

Harris, C.R., Millman, K.J., van der Walt, S.J., Gommers, R., Virtanen, P., Cournapeau, D., Wieser, E., Taylor, J., Berg, S., Smith, N.J., Kern, R., Picus, M., Hoyer, S., van Kerkwijk, M.H., Brett, M., Haldane, A., del Río, J.F., Wiebe, M., Peterson, P., Gérard-Marchant, P., Sheppard, K., Reddy, T., Weckesser, W., Abbasi, H., Gohlke, C., Oliphant, T.E., 2020. Array programming with NumPy. Nature 585 (7825), 357–362. http://dx.doi.org/10.1038/s41586-020-2649-2.

Hollmann, R., Merchant, C.J., Saunders, R., Downy, C., Buchwitz, M., Cazenave, A., Chuvieco, E., Defourny, P., de Leeuw, G., Forsberg, R., Holzer-Popp, T., Paul, F., Sandven, S., Sathyendranath, S., van Roozendael, M., Wagner, W., 2013. The ESA climate change initiative: Satellite data records for essential climate variables. Bull. Am. Meteorol. Soc. 94 (10), 1541–1552. http://dx.doi.org/10.1175/bams-d-11-00254.1.

Hoyer, S., Roos, M., Hamman, J., Keewis, Cherian, D., Fitzgerald, C., Fujii, K., Hauser, M., Maussion, F., Crusaderky, Clark, S., Kleeman, A., Kluyver, T., Munroe, J., Nicholas, T., Amici, A., Illviljan, Barghini, A., Banihirwe, A., Gimperiale, Zac Hatfield-Dodds, Bell, R., Abernathey, R., Johnomotani, Benoit Bovy, Roszko, M., Wolfram, P.J., Signell, J., Mühlbauer, K., 2021. pydata/xarray: v0.19.0. Zenodo, http://dx.doi.org/10.5281/ZENODO.598201.

Hunter, J.D., 2007. Matplotlib: A 2D graphics environment. Comput. Sci. Eng. 9 (3), 90–95. http://dx.doi.org/10.1109/mcse.2007.55.

Jordahl, K., Van Den Bossche, J., Fleischmann, M., McBride, J., Wasserman, J., Badaracco, A.G., Gerard, J., Snow, A.D., Tratner, J., Perry, M., Farmer, C., Hjelle, G.A., Cochran, M., Gillies, S., Culbertson, L., Bartos, M., Ward, B., Caria, G., Taves, M., Eubank, N., Sangarshanan, Flavin, J., Richards, M., Rey, S., Maxalbert, Bilogur, A., Ren, C., Arribas-Bel, D., Mesejo-León, D., Wasser, L., 2021. geopandas/geopandas: v0.10.0. Zenodo, http://dx.doi.org/10.5281/ZENODO.2585848.

Kerr, Y., Waldteufel, P., Wigneron, J.-P., Martinuzzi, J., Font, J., Berger, M., 2001. Soil moisture retrieval from space: the soil moisture and ocean salinity (SMOS) mission. IEEE Trans. Geosci. Remote Sens. 39 (8), 1729–1735. http://dx.doi.org/10.1109/36.942551.

Kottek, M., Grieser, J., Beck, C., Rudolf, B., Rubel, F., 2006. World map of the Köppen-Geiger climate classification updated. Meteorol. Z. 15 (3), 259–263. http://dx.doi.org/10.1127/0941-2948/2006/0130.

de Matthaeis, P., Lang, R.H., 2005. Microwave scattering models for cylindrical vegetation components. Prog. Electromagn. Res. 55, 307–333. http://dx.doi.org/10.2528/pier05040602.

McKinney, W., 2010. Data structures for statistical computing in python. In: Proceedings of the 9th Python in Science Conference. SciPy, http://dx.doi.org/10.25080/majora-92bf1922-00a.

Mengen, D., Jagdhuber, T., Balenzano, A., Mattia, F., Vereecken, H., Montzka, C., 2023. High spatial and temporal soil moisture retrieval in agricultural areas using multi-orbit and vegetation adapted sentinel-1 SAR time series. Remote Sens. 15 (9), 2282. http://dx.doi.org/10.3390/rs15092282.

Meurer, A., Smith, C.P., Paprocki, M., Čertík, O., Kirpichev, S.B., Rocklin, M., Kumar, A., Ivanov, S., Moore, J.K., Singh, S., Rathnayake, T., Vig, S., Granger, B.E., Muller, R.P., Bonazzi, F., Gupta, H., Vats, S., Johansson, F., Pedregosa, F., Curry, M.J., Terrel, A.R., Roučka, Š., Saboo, A., Fernando, I., Kulal, S., Cimrman, R., Scopatz, A., 2017. SymPy: symbolic computing in python. PeerJ Comput. Sci. 3, e103. http://dx.doi.org/10.7717/peerj-cs.103.

Moré, J.J., 1978. The Levenberg-Marquardt algorithm: implementation and theory. In: Numerical Analysis. Springer, pp. 105–116.

Mosello, B., 2015. The po river basin. In: How to Deal with Climate Change?. Springer International Publishing, pp. 81–116. http://dx.doi.org/10.1007/978-3-319-15389-6_4.

Naeimi, V., Elefante, S., Cao, S., Wagner, W., Dostálová, A., Bauer-Marschallinger, B., 2016. Geophysical parameters retrieval from sentinel-1 sar data: A case study for high performance computing at EODC. In: 24th High Performance Computing Symposium. Society for Modeling and Simulation International (SCS), http://dx.doi.org/10.22360/springsim.2016.hpc.026.

Nguyen, H.H., Cho, S., Jeong, J., Choi, M., 2021. A D-vine copula quantile regression approach for soil moisture retrieval from dual polarimetric SAR sentinel-1 over vegetated terrains. Remote Sens. Environ. 255, 112283. http://dx.doi.org/10.1016/j.rse.2021.112283.

Nicodemus, F.E., Richmond, J.C., Hsia, J.J., Ginsberg, I.W., Limperis, T., 1992. Geometrical considerations and nomenclature for reflectance. NBS Monogr. 160, 4.

Oh, Y., 2004. Quantitative retrieval of soil moisture content and surface roughness from multipolarized radar observations of bare soil surfaces. IEEE Trans. Geosci. Remote Sens. 42 (3), 596–601. http://dx.doi.org/10.1109/tgrs.2003.821065.

Pasquali, A., We acknowledge the work of Andrea Pasquali and the UMSUOL network team provided by the Agenzia Regionale Prevenzione Ambiente - Servizio Idro-Meteo-Clima (ARPA - SIMC) in support of the ISMN (http://www.arpa.emr.it/sim/).

Peng, J., Albergel, C., Balenzano, A., Brocca, L., Cartus, O., Cosh, M.H., Crow, W.T., Dabrowska-Zielinska, K., Dadson, S., Davidson, M.W.J., de Rosnay, P., Dorigo, W., Gruber, A., Hagemann, S., Hirschi, M., Kerr, Y.H., Lovergine, F., Mahecha, M.D., Marzahn, P., Mattia, F., Musial, J.P., Preuschmann, S., Reichle, R.H., Satalino, G., Silgram, M., van Bodegom, P.M., Verhoest, N.E.C., Wagner, W., Walker, J.P., Wegmüller, U., Loew, A., 2021. A roadmap for high-resolution satellite soil moisture applications – confronting product characteristics with user requirements. Remote Sens. Environ. 252, 112162. http://dx.doi.org/10.1016/j.rse.2020.112162.

PyTables Developers Team, 2002. PyTables: Hierarchical datasets in Python. URL: http://www.pytables.org/.

Quast, R., 2021. TUW-GEO/rt1: RT1 v1.5.1. Zenodo, http://dx.doi.org/10.5281/ZENODO.3745590.

Quast, R., 2022. raphaelquast/Eomaps: Eomaps v3.5. Zenodo, http://dx.doi.org/10.5281/ZENODO.6459599.

Quast, R., Albergel, C., Calvet, J.-C., Wagner, W., 2019. A generic first-order radiative transfer modelling approach for the inversion of soil and vegetation parameters from scatterometer observations. Remote Sens. 11 (3), 285. http://dx.doi.org/10.3390/rs11030285, URL: https://www.mdpi.com/2072-4292/11/3/285.

Quast, R., Wagner, W., 2016. Analytical solution for first-order scattering in bistatic radiative transfer interaction problems of layered media. Appl. Opt. 55 (20), 5379. http://dx.doi.org/10.1364/ao.55.005379.

Romshoo, S.A., Koike, M., Onaka, S., Oki, T., Musiake, K., 2002. Influence of surface and vegetation characteristics on C-band radar measurements for soil moisture content. J. Indian Soc. Remote Sens. 30 (4), 229–244. http://dx.doi.org/10.1007/bf03000366.

Service, C.C.C., 2019. ERA5-Land hourly data from 2001 to present. ECMWF, http://dx.doi.org/10.24381/CDS.E2161BAC.

Torres, R., Snoeij, P., Geudtner, D., Bibby, D., Davidson, M., Attema, E., Potin, P., Rommen, B., Floury, N., Brown, M., Traver, I.N., Deghaye, P., Duesmann, B., Rosich, B., Miranda, N., Bruno, C., L'Abbate, M., Croci, R., Pietropaolo, A., Huchler, M., Rostan, F., 2012. GMES sentinel-1 mission. Remote Sens. Environ. 120, 9–24. http://dx.doi.org/10.1016/j.rse.2011.05.028.

Ulaby, F., Moore, R., Fung, A.K., 1986. From Theory to Applications. Vol. 3, Microwave Remote Sensing: Active and Passive. Artech House Dedham, MA.

Virtanen, P., Gommers, R., Oliphant, T.E., Haberland, M., Reddy, T., Cournapeau, D., Burovski, E., Peterson, P., Weckesser, W., Bright, J., van der Walt, S.J., Brett, M., Wilson, J., Millman, K.J., Mayorov, N., Nelson, A.R.J., Jones, E., Kern, R., Larson, E., Carey, C.J., Polat, İ., Feng, Y., Moore, E.W., VanderPlas, J., Laxalde, D., Perktold, J., Cimrman, R., Henriksen, I., Quintero, E.A., Harris, C.R., Archibald, A.M., Ribeiro, A.H., Pedregosa, F., van Mulbregt, P., Vijaykumar, A., Bardelli, A.P., Rothberg, A., Hilboll, A., Kloeckner, A., Scopatz, A., Lee, A., Rokem, A., Woods, C.N., Fulton, C., Masson, C., Häggström, C., Fitzgerald, C., Nicholson, D.A., Hagen, D.R., Pasechnik, D.V., Olivetti, E., Martin, E., Wieser, E., Silva, F., Lenders, F., Wilhelm, F., Young, G., Price, G.A., Ingold, G.-L., Allen, G.E., Lee, G.R., Audren, H., Probst, I., Dietrich, J.P., Silterra, J., Webber, J.T., Slavič, J., Nothman, J., Buchner, J., Kulick, J., Schönberger, J.L., de Miranda Cardoso, J.V., Reimer, J., Harrington, J., Rodríguez, J.L.C., Nunez-Iglesias, J., Kuczynski, J., Tritz, K., Thoma, M., Newville, M., Kümmerer, M., Bolingbroke, M., Tartre, M., Pak, M., Smith, N.J., Nowaczyk, N., Shebanov, N., Pavlyk, O., Brodtkorb, P.A., Lee, P., McGibbon, R.T., Feldbauer, R., Lewis, S., Tygier, S., Sievert, S., Vigna, S., Peterson, S., More, S., Pudlik, T., Oshima, T., Pingel, T.J., Robitaille, T.P., Spura, T., Jones, T.R., Cera, T., Leslie, T., Zito, T., Krauss, T., Upadhyay, U., Halchenko, Y.O., and, Y.V.-B., 2020. SciPy 1.0: fundamental algorithms for scientific computing in python. Nature Methods 17 (3), 261–272. http://dx.doi.org/10.1038/s41592-019-0686-2.

Wagner, W., Bauer-Marschallinger, B., Navacchi, C., Reuß, F., Cao, S., Reimer, C., Schramm, M., Briese, C., 2021. A sentinel-1 backscatter datacube for global land monitoring applications. Remote Sens. 13 (22), 4622. http://dx.doi.org/10.3390/rs13224622.

Wagner, W., Hahn, S., Kidd, R., Melzer, T., Bartalis, Z., Hasenauer, S., Figa-Saldaña, J., de Rosnay, P., Jann, A., Schneider, S., Komma, J., Kubu, G., Brugger, K., Aubrecht, C., Züger, J., Gangkofner, U., Kienberger, S., Brocca, L., Wang, Y., Blöschl, G., Eitzinger, J., Steinnocher, K., 2013. The ASCAT soil moisture product: A review of its specifications, validation results, and emerging applications. Meteorol. Z. 22 (1), 5–33.

Zhu, L., Si, R., Shen, X., Walker, J.P., 2022. An advanced change detection method for time-series soil moisture retrieval from sentinel-1. Remote Sens. Environ. 279, 113137. http://dx.doi.org/10.1016/j.rse.2022.113137.